Annales
Geophysicae

Open Access

IMF-induced escape of molecular ions from the Martian ionosphere

Y. Kubota[1], K. Maezawa[1], H. Jin[2], and M. Fujimoto[1]

[1]Institute of Space and Astronautical Science, JAXA, Sagamihara, Japan
[2]National Institute of Information and Communications Technology, Koganei, Japan

Correspondence to: Y. Kubota (kubota@stp.isas.jaxa.jp)

Abstract. Since Mars does not possess a significant global intrinsic magnetic field, the solar wind interacts directly with the Martian ionosphere and can induce ion escapes from it. Phobos-2 and recent Mars Express (MEX) observations have shown that the escaping ions are O^+ as well as molecular O_2^+ and CO_2^+. While O^+ escape can be understood by the ion pick-up of non-thermal O corona extended around the planet, regarding the heavy molecular O_2^+ and CO_2^+, which are buried in the lower ionosphere, a novel escape mechanism needs to considered. Here we attack this problem by global magnetohydrodynamic (MHD) simulations. First, we clarify the global structure of the streamlines that result from the interaction with the solar wind. Then, by focusing on the streamlines that dip into the low-altitude part of the dayside ionosphere, we investigate the escape path of the molecular ions. The effects of the interplanetary magnetic field (IMF) on the molecular ion escape process are investigated by comparing the results with and without IMF. IMF has little effect on O^+ escape via ion pick-up mediated by solar wind electron impact ionization of the O corona. O_2^+ and CO_2^+ are shoveled from the low-altitude regions of the dayside ionosphere by magnetic tension in the presence of IMF. These ions are pulled by the U-shaped field lines to the north and south poles, and at the terminator, they are concentrated in the noon–midnight meridian plane. These ions remain confined to the noon–midnight plane as they are transported to the nightside to form the tail ray. Then they escape along the streamlines open to the interplanetary space. Under a typical solar wind and IMF condition expected at Mars, O^+, O_2^+ and CO_2^+ escape fluxes are 8.0×10^{23}, 3.5×10^{23} and 5.0×10^{22} ion s^{-1}, respectively, which are in good agreement with the MEX observations.

Keywords. Ionosphere (planetary ionospheres)

1 Introduction

The first detailed measurements of the magnetic field at Mars by the Mars Global Surveyor (MGS) (Acuña et al., 1998, 1999) has established that Mars, like Venus, does not have a large-scale magnetic field. Although localized strong magnetic fields of crustal origin have been discovered, the absence of large-scale magnetic field implies that the solar wind interaction with the Martian ionosphere would be Venus-like. Indeed, magnetic structures, such as magnetic field rotations at the ionopause and magnetic field, suggesting Venus-like interaction have been reported (Cloutier et al., 1999). In 1989 the Phobos-2 mission discovered O^+ outflow from Mars. The ion loss routes are either ion pick-up by the solar wind or accelerated beam (up to several keV) from the ionosphere. The estimated O^+ outflow rate is $\sim 3.0 \times 10^{25}$ s^{-1} (Lundin et al., 1989). The resent observations by Mars Express (MEX), which was launched in 2003 and carried an ion mass analyzer (IMA) onboard, has shown that the molecular ions of O_2^+ and CO_2^+ are also escaping from the ionosphere. The loss rates are 1.6×10^{23} s^{-1}, 1.5×10^{23} s^{-1} and 8.0×10^{22} s^{-1}, for O^+, O_2^+ and CO_2^+, respectively (Barabash et al., 2007a).

The purpose of this study is to understand the escape processes of molecular O_2^+ and CO_2^+ ions from the Martian ionosphere. For this, we need to understand (1) convection in the dayside low-altitude ionosphere, (2) transport of ionospheric plasma from dayside to nightside and (3) the structure of the nightside ionosphere. We believe that a global three-dimensional MHD simulation including a realistic ionosphere model, and that with sufficient spatial resolution in the low-altitude part of the ionosphere, is one of the best approaches to the problem. Below, crucial elements that show up in our study are reviewed.

Because simultaneous observations of magnetic field and charged particles have not been made in the Martian

ionosphere, a number of theoretical models for the solar-wind–ionosphere interaction of an unmagnetized body have been based on the observations at Venus. One of the prominent discoveries is the detection of large-scale magnetic field of solar wind origin in the dayside ionosphere well below the ionopause (Russell and Vaisberg, 1983). Ionopause is the plasma boundary between the solar wind and the ionospheric plasma. The interplanetary magnetic field (IMF) does not penetrate through this boundary in a "frozen-in" situation. The models developed to account for the formation mechanism of the large-scale magnetic field followed the "convection–diffusion" scenario. In this scenario, the key elements are the downward transport of magnetic flux from the ionopause region and the enhanced magnetic diffusion due to smaller conductivities in the lower ionosphere (Luhmann et al., 1984; Cravens et al., 1984; Phillips et al., 1984; Shinagawa et al., 1987; Shinagawa and Cravens, 1988; Shinagawa, 1996a,b). The model successfully reproduced the observed altitude profiles of the magnetic field that has a long enough decay time in order to explain the observations. However, they do not explain the reason why the downward transport is generated. Jin et al. (2008) discussed the relationship between the vertical convection and the solar wind dynamic pressure. Observationally, IMF penetration occurs when the solar wind dynamic pressure is relatively high. They suggested that the vertical convection is directed downward when an ion deficit occurs in the lower ionosphere. As the solar wind total pressure increases, the ionospheric pressure also increases in order to balance with the solar wind total pressure. The increase of the ionospheric pressure leads to an increased ionospheric electron density because the temperature at lower ionosphere does not almost change. The increase of the electron density leads to enhanced chemical loss of O_2^+ by recombination. Thus an ion deficit occurs in the lower ionosphere, and a downward flow from the ionopause occurs to compensate for the ion deficit in the lower ionosphere.

As for the observations of the Martian ionosphere, the Viking 1 and 2 landers are the only spacecraft that observed ion profiles in the ionosphere (Hanson et al., 1977), but they did not measure the magnetic field. MGS explored magnetic field structures globally in the low-altitude region. However, there has not been a detailed observation of IMF penetration into the ionosphere, because simultaneous charged particle observations are absent. According to the Viking observation, the ionospheric pressure at Mars is found to be insufficient to balance the solar wind dynamic pressure (Hanson and Mantas, 1988). Therefore, the case of Mars resembles that of Venus to some extent. Theoretical models show that the magnetic field of the solar wind origin penetrates into the Martian ionosphere and sustains the solar wind dynamic pressure (Shinagawa and Cravens, 1989; Jin, 2004).

Regarding the transport of the ionospheric plasma from dayside to nightside, Shinagawa (1996a,b) performed two-dimensional simulations for a Venus case. It was shown that the horizontal pressure gradient force is sufficient to produce the observed acceleration of ionospheric plasma from dayside to nightside, and the nightside ionosphere can be maintained by the plasma supply of this flow pattern. Because the simulated spatial range is 120–500 km, however, the upper part of the nightside region was out of the scope of the study.

The part of a field line embedded in the dayside stagnation region moves slowly, while those in the solar wind move at a rather fast speed. As a consequence, the magnetic field lines are stretched and draped around the planet. A three-dimensional simulation does take into account the magnetic tension force arising from this field-line deformation that is crucial for understanding the nightside ionosphere structure. Tanaka and Murawski (1997) first calculated the nightside structure of the Venus ionosphere by a three-dimensional MHD simulation that covered the altitude range from 140 km to 10 R_V (R_V: Venus radius) including a realistic ionosphere model. This simulation suggests that the O^+ ions from the ionosphere are transported to a few R_V altitude in the nightside, and then pulled anti-planetward by the magnetic tension.

Similarly, a Martian case has been simulated by Ma et al. (2004). The three-dimensional MHD simulation included a realistic ionosphere and the crustal field. The nightside structure of the Martian ionosphere, however, was not the focus of the study.

Various hybrid simulation studies have been made of the solar-wind–ionosphere interaction of unmagnetized planets (Modolo et al., 2006, 2005; Bößwetter et al., 2004; Kallio and Janhunen, 2002, 2001; Shimazu, 2001, 1999; Brecht, 1997; Brecht et al., 1993). The hybrid simulations treat ions as particles while electrons are considered as a massless charge-neutralizing fluid. The hybrid simulations do have the advantage of including ion kinetic effects. These simulations, however, did not incorporate realistic ionosphere models, and the grid resolution in the ionosphere has been relatively low; that is, the radial grid size is typically ∼ 100 km in the ionosphere. Using a hybrid model, it has been difficult to study the convection in the lower ionosphere, which is the crucial element for understanding the molecular ion loss from Mars, and where the importance of the ion kinetic effects is minimal because of the collisional nature of the local plasma.

These lead us to think that a global three-dimensional MHD simulation including a realistic ionosphere model, and that with sufficient spatial resolution in the lower ionosphere, is one of the best approaches to understand the molecular ion escape from the Martian ionosphere. Indeed Ma and Nagy (2007) calculated ion escape fluxes by using a multispecies three-dimensional MHD simulation code including a realistic ionosphere. This code included ionospheric processes such as ion production and loss due to photochemical reactions, gravity and collisions with neutral atmosphere, with a sufficiently small (10 km) radial grid spacing in the ionosphere. The estimated escape fluxes of O^+, O_2^+ and CO_2^+ are

7.2×10^{23}, 1.9×10^{23} and 1.3×10^{23} ion s^{-1}, respectively, under a solar minimum condition. While the estimated escape fluxes are consistent with the MEX observations, Ma and Nagy (2007) did not elucidate the ion escape mechanism. Najib et al. (2011) calculated ion escape fluxes by using a multifluid three-dimensional MHD simulation code that treats asymmetry due to the convection electric field included in the ionosphere process with a small (10 km) radial grid spacing in the same way as Ma and Nagy (2007). The estimated O_2^+ escape flux is higher than that of Ma and Nagy (2007) compared to the escape rates of the other species. They discuss that this higher escape flux might be due to the new dynamics observed through their model as asymmetric plumes. However, Najib et al. (2011) did not elucidate the ion escape mechanism.

In this paper, we discuss the ion escape mechanism of the molecular ions such as O_2^+ and CO_2^+. Ions of O_2^+ and CO_2^+ are mainly produced in the lower ionosphere. Therefore, in order to have these ionospheric molecular ions to escape by a large amount, the ions produced at such low altitudes need to be transported upward to reach the altitudes where ions find themselves on streamlines that are open to the interplanetary space. We will show that the presence of finite IMF and its magnetic tension in the dayside part is crucial for the escape of these two ion species from Mars.

2 Simulation model

2.1 Governing equations

A set of three-dimensional multispecies MHD equation is developed, which includes the continuity equations separately for H^+, O^+, O_2^+ and CO_2^+ ions, a common momentum equation, Maxwell's equations and the energy equation. These equations are summarized below:

$$\frac{\partial}{\partial t}\rho_s + \frac{\partial}{\partial \boldsymbol{r}}(\rho_s \boldsymbol{u}) = S_a, \tag{1}$$

$$\frac{\partial}{\partial t}\rho \boldsymbol{u} + \frac{\partial}{\partial \boldsymbol{r}}\{\rho \boldsymbol{u}\boldsymbol{u} - \frac{1}{\mu_0}\boldsymbol{B}\boldsymbol{B} + \left(p + \frac{B^2}{2\mu_0}\right)\boldsymbol{I}\} = S_b, \tag{2}$$

$$\frac{\partial}{\partial t}\boldsymbol{B} - \mathrm{rot}(\boldsymbol{u} \times \boldsymbol{B}) = S_c, \tag{3}$$

$$\frac{\partial}{\partial t}\frac{p}{\gamma - 1} + \frac{\partial}{\partial \boldsymbol{r}}\left(\frac{\gamma}{\gamma - 1}p\boldsymbol{u}\right) - \boldsymbol{u}\frac{\partial p}{\partial \boldsymbol{r}} = S_d, \tag{4}$$

where ρ_s is the mass density for the s ion component ($s = H^+$, O^+, O_2^+ and CO_2^+), ρ is the total mass density, $\boldsymbol{u}$ is the common velocity, $\boldsymbol{B}$ the magnetic field and p the total thermal pressure. γ is the ratio of specific heats (and taken to be 7/5). μ_0 is the magnetic permeability.

The source terms are

$$S_a = m_s \alpha_s - \beta_s \rho_s, \tag{5}$$

$$\boldsymbol{S}_b = -\frac{GM\rho}{r^2}\frac{\boldsymbol{r}}{r} - \nu_{\mathrm{in}}\rho\boldsymbol{u} - \sum_s \beta_s \rho_s \boldsymbol{u}, \tag{6}$$

$$\boldsymbol{S}_c = D_B \Delta \boldsymbol{B}, \tag{7}$$

$$S_d = \frac{1}{\gamma - 1}\sum_s \alpha_s k_B T_0(h) - \frac{1}{\gamma - 1}\sum_s \beta_s \frac{N_s}{N_e}p, \tag{8}$$

where α_s is the photochemical production rate per volume, m_s is the mass per particle, β_s is the chemical loss rate per particle for ion species s, G is the gravity constant, M is the mass of the planet, ν_{in} is the ion-neutral collision frequency, D_B is the magnetic diffusion coefficient, k_B is the Boltzmann constant, and $T_0(h)$ is the assumed temperature of newly produced plasma as a function of altitude based on the Viking lander observations (Hanson and Mantas, 1988). This temperature model is shown in Fig. 1. N_s is the number density of ion species s ($N_s = \rho_s/m_s$) and N_e is the electron density that we assumed to be equal to the sum of N_s. The ion-neutral collision frequency was set at $\nu_{\mathrm{in}} = 1.0 \times 10^{-9}$ $\{[O]+[CO_2]+[H]\}$ s^{-1}. The diffusion coefficient is expressed as $D_B = m_e(\nu_{\mathrm{en}} + \nu_{\mathrm{ei}})/\mu_0 N_e e^2$, where m_e is the electron mass, ν_{en} electron-neutral collision frequency, ν_{ei} electron–ion collision frequency and e the electron charge. ν_{ei} and ν_{en} are given as $\nu_{\mathrm{ei}} = 54.5 \times N_e/T_e^{3/2}$ s^{-1} (T_e, the electron temperature) and $\nu_{\mathrm{en}} = 3.68 \times 10^{-8}[CO_2]$ s^{-1}, respectively (both taken from Schunk and Nagy, 2000). We replaced T_e with the plasma temperature T_p ($T_p = p/N_e/k_B/2$) since we did not separate ion and electron temperatures in the present model.

2.2 The neutral environment and photochemical reactions

Neutral atmospheric profiles are necessary for calculating ion production and loss rates due to photochemical reactions, and ion-neutral and electron-neutral collision frequencies. The neutral atmosphere has the thermal components and the non-thermal component. The non-thermal component is represented by oxygen atoms that are produced by the dissociative recombination of molecular ions O_2^+. The radial variation of the number density in the gravity field of the planet can be expressed as

$$n_i(h) = n_i(h_0)\exp\left[\frac{GMm_i}{k_B T_i}\left(\frac{1}{R_M + h} - \frac{1}{R_M + h_0}\right)\right], \tag{9}$$

where $n_i(h)$ is the number density at the height h for the i neutral component ($i = H$, O, CO_2), T_i is the neutral temperature. The equivalent temperature of non-thermal O is assumed to be 2900 K. The density of the non-thermal oxygen
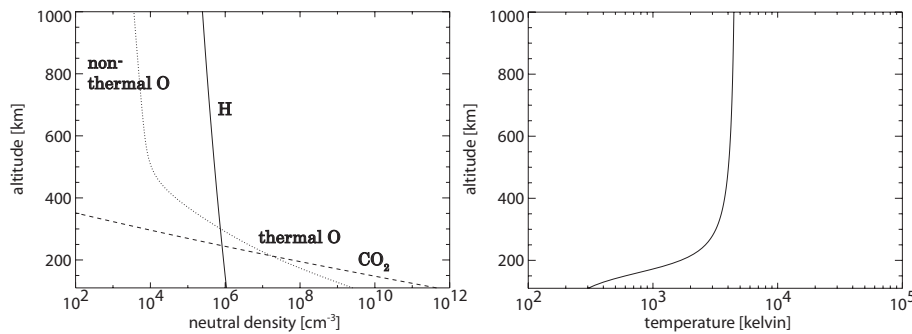
Fig. 1. The neutral atmosphere profiles (left) and the temperature profile (right) used in the present model.

atom at the altitude ($h_0 = 400$ km) was set at 1.0×10^4 cm^{-3}. This radial profile is consistent with the profile of Kim et al. (1998) that was obtained by a Monte Carlo simulation. The thermal components are composed of H, O and CO$_2$. The same constant temperature of 200 K is assumed for the altitude higher than 200 km. The neutral densities at the altitude $h_0 = 200$ km were set to 1.5×10^7 cm^{-3} for O, 3.0×10^7 cm^{-3} for CO$_2$ and 9.0×10^5 cm^{-3} for H. At altitudes lower than 200 km, the density profiles of H, O and CO$_2$ were taken from Krasnopolsky (1993) for a solar minimum condition. The altitude profiles of the temperatures model are from Krasnopolsky and Gladstone (1996). The neutral atmosphere model used in this study is shown in Fig. 1.

In the present model, photochemical reactions for four ion species (H$^+$, O$^+$, CO$_2^+$ and O$_2^+$) are taken into account. The considered photochemical reactions and their reaction coefficients are listed in Table 1. The photoionization frequencies at Mars were set at 1.0×10^{-7} s^{-1} for O$^+$ and 2.6×10^{-7} s^{-1} for CO$_2^+$ under a solar minimum condition, which were taken from Torr and Torr (1985) for Earth's case and adjusted to the heliocentric distance of Mars. The absorption of EUV flux by the neutral atmosphere is included in the model. The photoionization frequencies are assumed to depend on solar zenith angle as $\propto \cos(\text{SZA})$. Reaction rates with solar wind protons and electrons need special care because they depend strongly on the temperature of incident ions and electrons. Reaction rates and average energy of ejected particles for the proton-neutral charge exchange (CE) and for the electron impact ionization (EII) reactions are obtained by Monte Carlo simulations, whose details are given in Jin et al. (2006).

2.3 Numerical method

A triangular grid has been generated on spherical surfaces. In the construction process of the grid system, it is desirable that two-dimensional spherical surfaces are covered by control volumes of similar size, because the integration time step is restricted by the smallest control volume. The number of grids on the spherical surfaces is 8000, which corresponds to 93 km × 93 km at the inner boundary. The altitude range

Table 1. List of chemical reaction and rates considered in the model. Units are cm^3 s^{-1}. The reaction coefficients for the ion-neutral charge exchange (Reactions R1, R2 and R4) were taken from Anicich (1993), those for the recombination (Reactions R5 and R6) were taken from Schunk and Nagy (2000) and those for the proton-neutral charge exchange (Reactions CE1 and CE2) and for the electron impact ionization (Reactions EII1 and EII2) were taken from Jin et al. (2006).

No	Reaction	Rate coefficient
	$CO_2 + h\nu \rightarrow CO_2^+ + e$	
	$O + h\nu \rightarrow O^+ + e$	
(R1)	$CO_2^+ + O \rightarrow O^+ + CO_2$	$2.60 \times 10^{-10} \times 0.37$
(R2)	$O^+ + CO_2 \rightarrow O_2^+ + CO$	1.10×10^{-9}
(R3)	$O^+ + H \rightarrow H^+ + O$	$9/8 \times$ (CE2)
(R4)	$CO_2^+ + O \rightarrow O_2^+ + CO$	$2.60 \times 10^{-10} \times 0.63$
(R5)	$CO_2^+ + e^- \rightarrow CO + O$	$3.1 \times 10^{-7} \times (300/T_e)^{0.5}$
(R6)	$O_2^+ + e^- \rightarrow O + O$	$1.95 \times 10^{-7} \times (300/T_e)^{0.7}$
		for $T_e < 1200$ K
		$7.38 \times 10^{-8} \times (1200/T_e)^{0.56}$
		for $T_e > 1200$ K
(CE1)	$H^+ + H \rightarrow H^+ + H$	Jin et al. (2006)
(CE2)	$H^+ + O \rightarrow O^+ + H$	Jin et al. (2006)
(EII1)	$H + e^- \rightarrow H^+ + e^- + e^-$	Jin et al. (2006)
(EII2)	$O + e^- \rightarrow O^+ + e^- + e^-$	Jin et al. (2006)

of the simulated region is from 120 km (the bottom of the ionosphere) to 12 R_M (R_M: Mars radius). By changing bin size along the radial direction, Tanaka and Murawski (1997) numerically simulated the solar-wind–Venus interaction with sufficient resolutions for the entire region of interaction including the formation of the bow shock and detailed interaction processes occurring in the ionosphere. A similar idea was adopted in the present model in treating both the ionosphere and the boundary region with sufficient spatial resolutions ($\Delta r = 10$–4967 km). To solve the MHD equations, the Lax–Wendroff scheme was used. This scheme has a second-order accuracy both in time and space, but generates numerical oscillations near discontinuities and shocks. Therefore numerical diffusion is required to suppress the oscillations. In the present calculation, numerical oscillations were kept at

minimum by controlling the coefficients of numerical diffusion, which are of the third order as compared to the second-order numerical accuracy of the Lax–Wendroff code. For the outer boundary, the variables were fixed at the solar wind values (as given in Sect. 2.4) at the upstream boundary. Free boundary conditions are used for the downstream boundary. For the inner boundary at the bottom of the ionosphere, the vertical plasma velocity was assumed to vanish, and the magnetic field magnitude was also assumed to vanish.

2.4 Solar wind parameters

For simulations with finite IMF, the solar wind parameters are as follows: plasma density of $n_{sw} = 3.0 \, cm^{-3}$, velocity of $V_{sw} = 400 \, km \, s^{-1}$, magnetic field of $B_{sw} = 4.0 \, nT$ and temperature of $T_{sw} = 1.0 \times 10^5 \, K$. The direction of IMF was assumed to be perpendicular to the solar wind flow. To clarify the role of IMF in the molecular ion escape process, comparison between the cases with and without IMF is made. In the case of no IMF, the solar wind parameters are chosen such that the total pressure, the velocity and the temperature in the post-shock region are the same as the corresponding value from the finite IMF case. Jin (2004) suggests that IMF penetration into the ionosphere occurs when the solar wind total pressure is relatively high. The present solar wind condition enables IMF to penetrate into the ionosphere.

3 Simulation results

The system was allowed to develop in time, and eventually a steady state was obtained. Figure 2 shows how IMF lines deform as they interact with the Martian ionosphere. The figure also shows the coordinate system: The solar wind flow is toward $-x$ direction. The IMF is directed in the $+y$ direction and the z axis completes the right-handed coordinate system. The x-y plane (the $z = 0$ plane) is called the equatorial plane, and the x-z plane (the $y = 0$ plane) is called the meridian plane hereafter.

The field line in panel (a) is at $z = 1 \, R_M$ initially. With this shallow impact, the field line is only weakly bent as it is convected anti-sunward. On the other hand, the field line shown in panel (b), which initially has $z = 0.1 \, R_M$, impacts deep into the ionosphere. Then the part of the field line embedded inside the ionosphere is slowed down so greatly that this part is delayed substantially from its ends in the solar wind. This results in significant bending of the field line – that is, the U-shaped field line shown in the panel. The field line exerts magnetic tension on the ionospheric plasma. This is one of the key elements of the present study.

3.1 The Martian nightside density structure

In our simulation, we obtain the densities of four ion species (H^+, O^+, O_2^+ and CO_2^+) by integrating the equation of continuity for each species. Each density distribution shows dif-
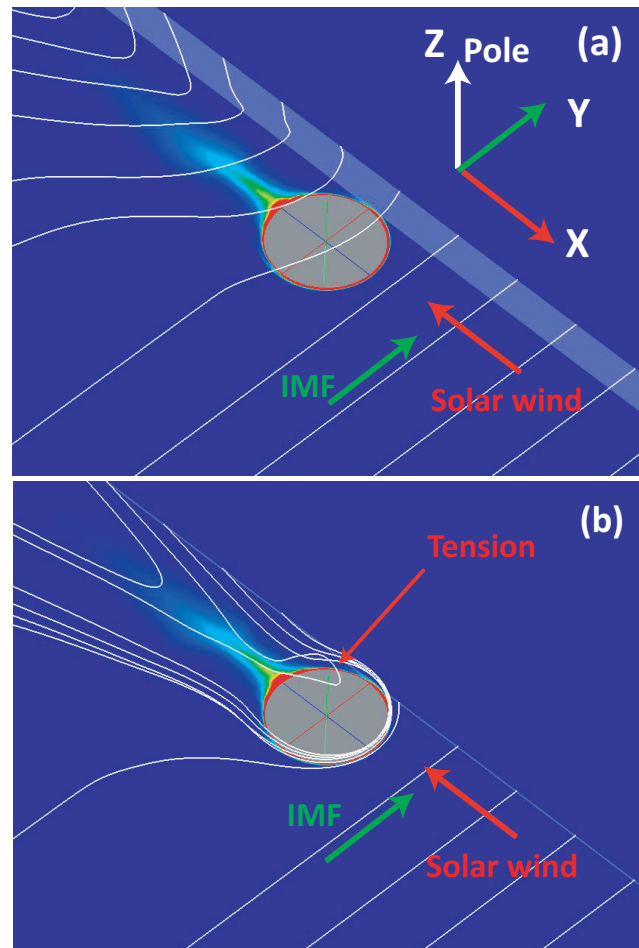

Fig. 2. The distribution of O_2^+ density is shown by color contours, and the three-dimensional configuration of magnetic field lines is shown by white lines. The direction of the solar wind flow is toward $-x$ direction. The IMF is directed in the $+y$ direction and the z axis completes the right-handed coordinate system. The field line in panel **(a)** is at $z = 1 \, R_M$ initially. The field line in panel **(b)** is at $z = 0.1 \, R_M$ initially.

ferent structures as shown in Fig. 3. The top half of each panel shows the meridian plane, while the bottom half shows the equatorial plane. We used a multispecies MHD model. Therefore our model results are plane symmetry; that is, the $z > 0$ result is a mirror image of the $z < 0$ result, and the $y > 0$ result is a mirror image of the $y < 0$ result. A ray structure can be recognized at the center of the tail. The ions in the tail ray are composed of, in orders of decreasing density, H^+, O_2^+, O^+ and CO_2^+.

Figure 4 shows the altitude profiles of the ion densities at the subsolar point. We compare our density distribution with Viking 1 lander observation in Sect. 4. There are peaks of H^+ and O^+ at $\sim 240 \, km$ altitude. The peak of H^+ is created by the chemical reaction in the ionosphere. The heavy ions such as O_2^+ and CO_2^+ are produced at the low-altitude region, and the densities are peaked at $\sim 120 \, km$ altitude. While the
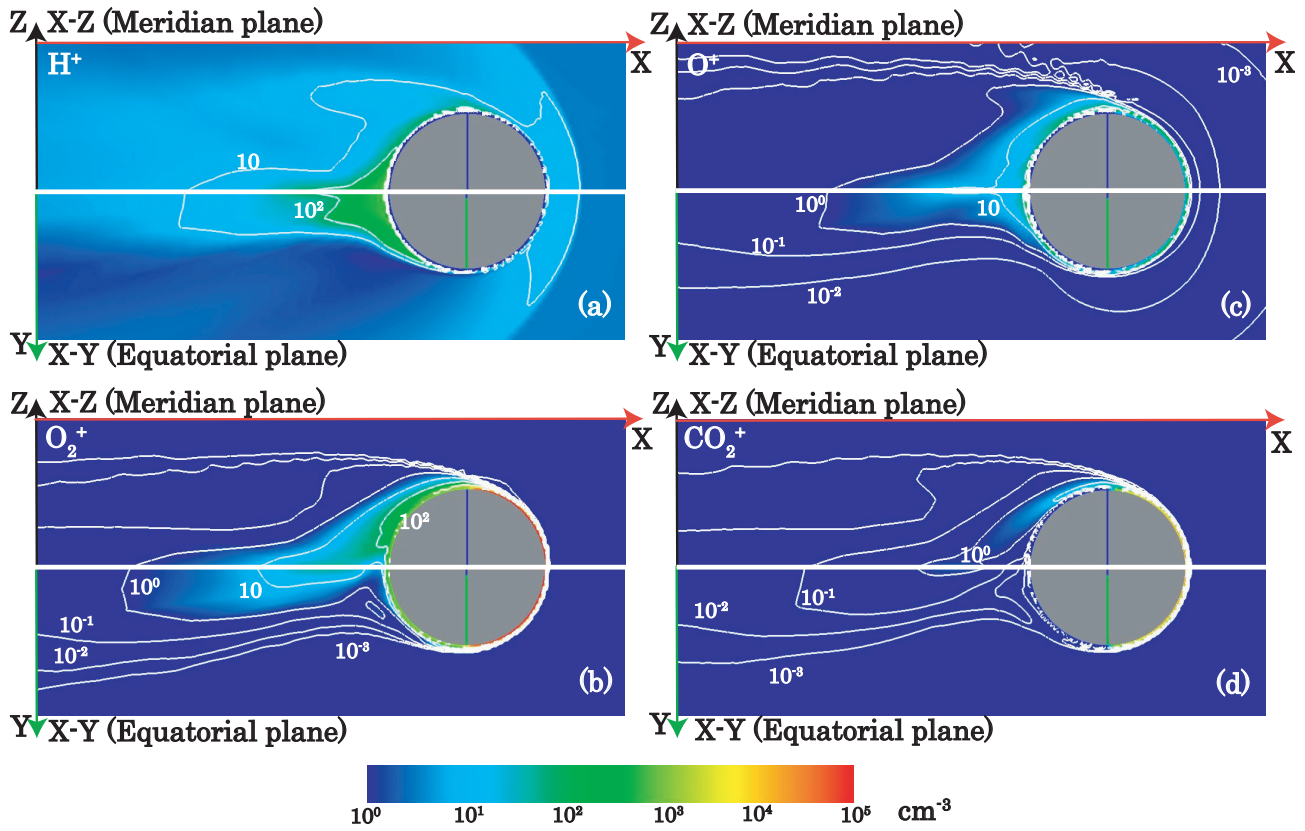
Fig. 3. The distribution of H^+ (top left), O^+ (top right), O_2^+ (lower left) and CO_2^+ (lower right) densities shown by color contours. The solar wind flows from the right. The top half of each panel represents the meridian plane, while the bottom half represents the equatorial plane.
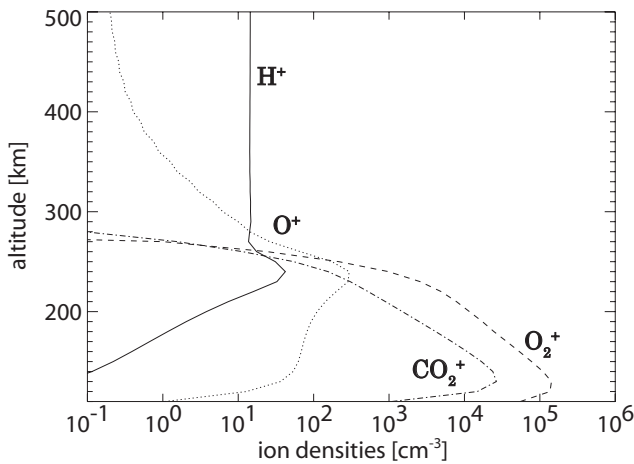

Fig. 4. The altitude profiles of the ion densities at the subsolar point.

dayside profile shown in Fig. 4 shows that the molecular O_2^+ is distributed at lower altitudes than O^+, the tail ray structure shown in Fig. 3 indicates that O_2^+ shows a pronounced extended feature – first (at lower altitude) in the meridian plane (top) and then in the equatorial plane (bottom), into the night-

side. The same is seen for CO_2^+. To transport O_2^+ and CO_2^+ to high altitude on the nightside, O_2^+ and CO_2^+ need to be shoveled from the lower ionosphere in the dayside and accelerated into the tail ray. It is this mechanism that will be studied in this paper.

In order to understand the role of the solar wind magnetic field in the molecular ion transport, we show the density distribution of O_2^+ and O^+ obtained in the case without IMF in Fig. 5. Comparison with Fig. 3 shows the following: (1) along the tail axis at $1\,R_M$ altitude, O_2^+ density is less than $0.1\,cm^{-3}$ for the case without IMF. The O_2^+ density at the same location for the case with IMF is $10\,cm^{-3}$, implying 2 orders of magnitude reduction in the molecular ion density at the high-altitude position in the tail. That is, the ray structure of O_2^+ forms only in the presence of IMF. (2) O_2^+ starts to be elevated to higher altitude already at the terminator for the case with IMF, while such a signature is absent in the case without IMF. This implies that only in the presence of IMF is O_2^+ shoveled from the dayside lower ionosphere and transported to higher altitude in the meridian plane as they are convected tailward with the bent field line. (3) In contrast, regarding O^+, the density pattern from the case without IMF shows a similar pattern to that on the equatorial plane from the case with IMF (Fig. 3c, bottom).
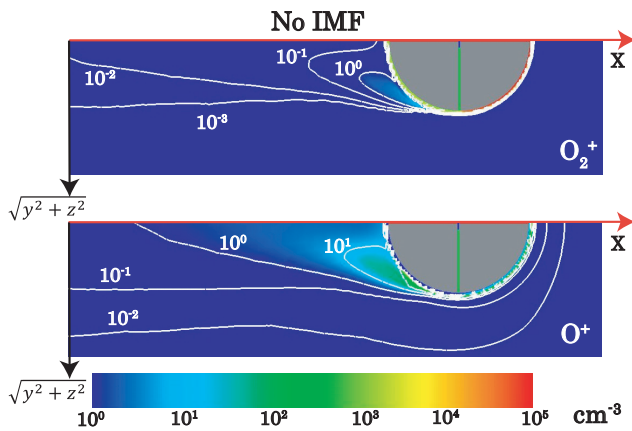
Fig. 5. The distribution of O_2^+ and O^+ density for the case without IMF. The vertical axis is $\sqrt{y^2 + z^2}$ because of x-axial symmetry.

3.2 The ion flow pattern leading to the ray structure

Figure 6 compares the nightside density distribution of O_2^+ with the flow pattern. The flow pattern in the meridian plane is heavily affected by magnetic tension. O_2^+ elevated to higher altitude upon crossing the terminator is shifted towards the equatorial plane in the nightside. The pair of flows from north and south collide on the tail axis at $0.5\,R_M$ above the surface. Then the converging flows are redirected to the anti-sunward direction.

One can also see that, in the equatorial plane, there is little connection between the low-altitude O_2^+ in the nightside ionosphere and the O_2^+ at higher altitude forming the tailward jetting ray. We conclude that the transport of the heavy ions in the meridian plane from dayside to nightside is crucial for forming the anti-sunward-flowing ray in the tail. Since the ions in the ray are eventually lost into the interplanetary space, the ray formation is the process that causes the heavy molecular ions to be lost from the planet.

What is missing in the above argument is the flow pattern in the dayside, which is now shown in Fig. 7. Color contours for V_X, V_Y and V_Z at the ionospheric altitude of 400 km are shown. The tailward flow ($V_X < 0$ and $V_Z > 0$ in the Northern Hemisphere) converges towards the meridian plane ($V_Y > 0$ on the $Y < 0$ side, and vice versa) at SZA > 75°. This flow pattern is created as the ions are accelerated by the magnetic tension of a U-shaped field line whose apex is embedded in the ionosphere. In a sense, one may say that the escaping ionospheric ions are dragged by the solar wind ions. However, because the momentum exchange is mediated by the deformed field lines, the process involves the formation of the tail ray. Figure 8 shows the resultant O_2^+ density concentration on the meridian plane at the terminator. The flow pattern of these concentrated O_2^+ beyond the terminator is what has been discussed in the previous paragraph (Fig. 6).

In order to see where the O_2^+ in the tail ray originates, we shown in Fig. 9 the distribution of O_2^+ flux (color) at the ionospheric altitudes. The horizontal axis is SZA and the vertical axis is the altitude. Here we focus on the altitude range from 100 to 850 km. The top panel shows the meridian plane. The bottom panel shows the equatorial plane. The black lines in the top and the bottom panels are the demarcation lines between the open and the closed streamlines. Here we define the topology of stream lines as follows. Stream lines that are connected to infinity of downstream are defined to be "open". Thus particles forming O_2^+ flux on the open region escape to the interplanetary space. The lines that have ends in the ionosphere are defined to be "closed". Particles forming O_2^+ flux on the close region do not escape, because the stream lines are connected to the ionosphere. Of course, we assume here that the simulation has already reached a quasi-steady state.

Comparison of two panels shows that the O_2^+ flux in the x-z (meridian) plane is much larger than the x-y (equatorial) plane. O_2^+ is produced at a low altitude of 200 km. In the x-y plane, O_2^+ production region is not on the open region but is connected to the lower ionosphere. In the x-z plane, the O_2^+ production region at 200 km is in the open region. Produced O_2^+ on the open stream lines are accelerated by the magnetic tension and escape to the interplanetary space. This O_2^+ flux creates the molecular tail-ray structure.

3.3 Quantifying the ion escape flux

In MHD simulations, the ion escape rate is usually estimated by numerically integrating the escaping ion flux across a plane placed perpendicular to the solar wind at a reasonably large distance behind the planet (Ma and Nagy, 2007). This method is hereby called Method 1. We, however, found that this method tends to give a value larger than the one estimated independently from the chemical balance between the ion production and loss rates. The reason is the following: in MHD simulations, an artificial viscosity should be included to avoid numerical oscillations. The artificial relaxation tends to be large at a sharp boundary, one of which is the one between the stagnant ionospheric plasma and the flowing solar wind plasma. This region is the key to determining the molecular ion process. Indeed, the escape fluxes in the cases without IMF (Table 2) are $\sim 10^{22}\,\mathrm{s}^{-1}$ in the case where 10 km is the minimum grid size, and $\sim 10^{23}\,\mathrm{s}^{-1}$ in the case of 20 km. Therefore we decided to estimate the ion escape flux using another method as well.

Here we introduce the idea of calculating the ion escape flux that is less vulnerable to the artificial diffusion. This method, which is called Method 2 hereafter, is as follows. In the steady state that we are dealing with, the ion escape flux F_j can be also calculated by

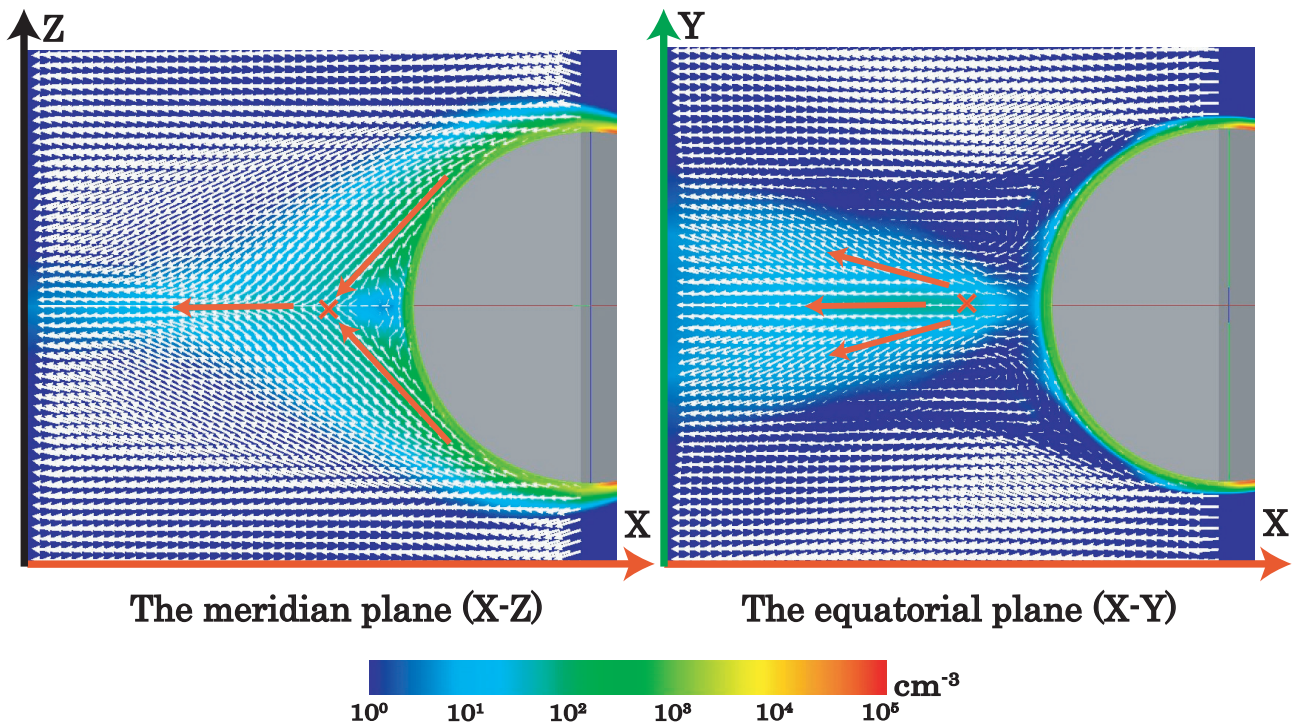$$F_j = \int_0^V \left[Q_j - L_j \right] dV, \tag{10}$$

Fig. 6. The distribution of O_2^+ density (color) superposed by the velocity vectors (white arrows). The solar wind flows from the right. The left panel represents the meridian plane, while the right panel represents the equatorial plane.
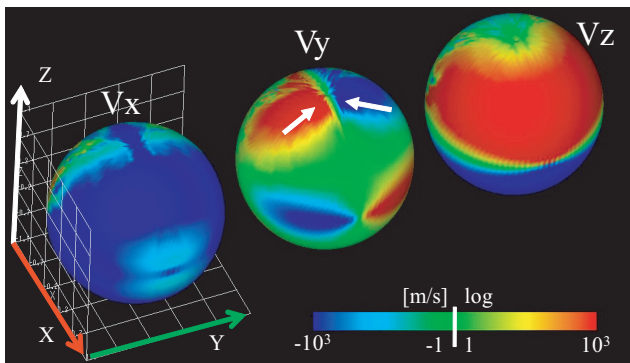

Fig. 7. The velocity components at the altitude of 400 km in the dayside ionosphere. From left to right, V_X, V_Y and V_Z.

where V is volume, Q_j is the ion production rate and L_j is the chemical loss rate for ion species j. The crucial point here is that the integration should be made only over the volume through which the streamlines that are open to the interplanetary space pass. The ionospheric ions can escape only if they are situated on these streamlines. If the integration is made over the whole simulation box, we cannot distinguish the ion escape flux from the artificial diffusion flux. Method 2 is less damaged by the worst effect of the artificial viscosity that brings fluxes on a closed streamline onto an open streamline via diffusion in the direction perpendicular to the streamline. The interface between a closed and an open streamline tends to be associated with enhanced velocity shear and thus more vulnerable to the artifact.

Table 2 compares ion escape fluxes estimated by using Methods 1 and 2 and those obtained by MEX observations. In the case of no IMF, the escape fluxes of O_2^+ and CO_2^+ are negligible when calculated by Method 2, while they are estimated to be significant by Method 1. The values obtained by Method 2 have very small absolute values of less than $10^{18} \, \text{s}^{-1}$ and a negative sign. We note that the escape flux calculated by Method 2 can become negative. There are ions that come onto the open streamlines by artificial diffusion and that are lost via chemical reactions. If this artificial loss is more than the integration of the source term along the open streamlines (which is $\sim 10^{14} \, \text{s}^{-1}$ in this case), the flux is calculated to be negative. That is, the numerical diffusion tends to reduce the estimated escape flux by Method 2, while it tends to increase the estimated flux by Method 1. The true escape flux should be on the order of, or less than $\sim 10^{14} \, \text{s}^{-1}$, which is negligible as compared to the estimate by Method 1 (Table 2). On the other hand, in the case of simulation with a finite IMF, O_2^+ and CO_2^+ escape fluxes obtained independently by Methods 1 and 2 are in reasonably good agreement (the largest difference is the factor of 2 for the O_2^+ flux). We consider that errors due to the artificial diffusion coming into these escape flux estimates are within the acceptable range.
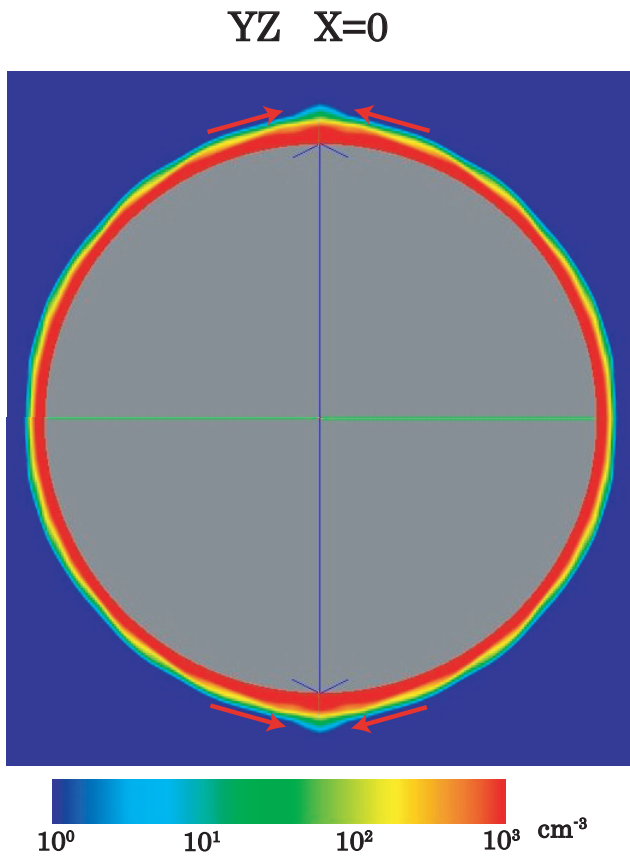
YZ X=0

Fig. 8. The O_2^+ density pattern on the $x = 0$ plane.

Fig. 9. Contour plots of the O_2^+ flux distribution. The horizontal axis is in the solar zenith angle and the vertical axis is the altitude. Here we are focusing into the ionospheric altitude. The flow patterns are superposed by the white arrows. The top panel shows the meridian plane, and the bottom panel shows the equatorial plane. The label "open" ("closed") indicates the region that is filled by open (closed) streamlines. The black lines in the top and the bottom panels are the demarcation lines between these two regions.

Table 2. List of the ion escape flux [s^{-1}]. The ion escape fluxes of the observation were taken from Barabash et al. (2007a).

	Δr	O^+	O_2^+	CO_2^+
Method 1 (no IMF)	10 km	1.2×10^{24}	1.2×10^{22}	3.9×10^{20}
Method 2 (no IMF)	10 km	6.4×10^{23}	~ 0	~ 0
Method 1 (finite IMF)	10 km	1.1×10^{24}	6.4×10^{23}	4.8×10^{22}
Method 2 (finite IMF)	10 km	8.0×10^{23}	3.5×10^{23}	5.0×10^{22}
Observation		1.6×10^{23}	1.5×10^{23}	8.0×10^{22}
Method 1 (no IMF)	20 km	1.1×10^{24}	1.3×10^{23}	3.0×10^{21}

Now we discuss the ion loss rate obtained by Method 2. In the presence of IMF, it is found that O_2^+ and CO_2^+ escape flux are 3.5×10^{23} s^{-1} and 5.0×10^{22} s^{-1}, respectively. These values are in relatively good agreement with the MEX observation. The molecular ion loss rates are negligible in the absence of IMF, which indicates that the shoveling from the dayside lower ionosphere and acceleration into the tail ray require the magnetic tension. The escape flux of O^+ is rather insensitive to IMF. This fact is consistent with the interpretation that most of the escaping O^+ are produced by ionizations of the non-thermal O corona that is extended to very high altitudes. Note that the ionized O^+ is not accelerated by the convection electric field in the case without IMF. However, 62 % of non-thermal O made by the dissociative recombination of O_2^+ has more than 2 eV, which is the energy of escape velocity for oxygen (Nagy and Cravens, 1988). Therefore we consider that O^+ has more than 2 eV after non-thermal O is ionized. O^+ can escape because O^+ has more than 2 eV. The magnetic tension effects are crucial for the dynamics in the dayside lower ionosphere and in lifting the streamlines into the tail ray. While most of the molecular ions escape along this path, O^+ are already on the solar-wind-like streamlines when they are ionized. Indeed, a step in Method 2 allows us to confirm that the O^+ escape rate is sufficiently provided by
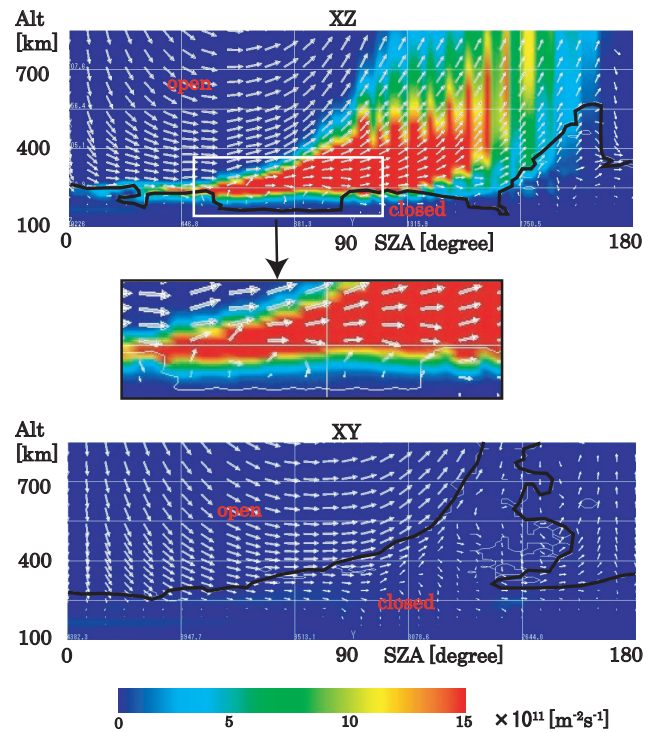
ionization of the O corona above 250 km altitude. The O^+ escape flux is 8.0×10^{23} s^{-1} in the case of finite IMF, which is larger than the MEX observations by a factor of 5. At this stage, in the lack of further detailed information, we would judge this as reasonable agreement.

3.4 Molecular ion production on open streamlines

From the arguments deployed above, it is now clear that, for the molecular O_2^+ to escape, the crucial issue is how to situate the molecular ion production region ($Q_{O_2^+}$) on the open

streamlines. In order to clarify this better, we plot in Fig. 10 the color contour of the O_2^+ production/loss rates. The horizontal axis is SZA, while the vertical axis is the altitude. The three panels show no IMF case (top), the equatorial plane for the case with IMF (middle) and the meridian plane for the case with IMF (bottom), respectively.

As shown in the top panel, the O_2^+ production region is located at the altitude of 200 km in the dayside. The produced O_2^+ are transported downward and are subject to the loss process at the altitude of 150 km, where the recombination reaction of Reaction (R6) in Table 1 occurs (Jin et al., 2008). In the nightside, the O_2^+ production region is located in a thin region at the altitude 200 km. The production is due to the precipitation of O^+ from higher altitude. O^+ impact to neutral CO_2 at the altitude of 200 km and O_2^+ is generated by the Reaction (R2). Also shown in Fig. 10 are the flow vector (white) and the open/closed demarcation line. In the absence of IMF, the open/closed boundary is located above 400 km altitude – that is, far above the altitude of the O_2^+ production region (top). We have seen that O_2^+ escapes little in such cases because the production region is not embedded in the region of "open" streamlines.

When IMF is present, the field lines are deformed to exert tension force on the ionospheric plasma. In particular, magnetic tension changes the flow direction on the nightside from planetward to anti-planetward. This shifts the open/closed boundary downward in the equatorial plane as shown in the middle panel. This, however, is not enough to make it touch the O_2^+ production region. Note that the magnetic tension effects are smallest on the equatorial plane.

In the bottom panel, the O_2^+ production region (colored red) is located at about 200 km altitude on the dayside. The open/closed boundary is located at the altitudes of 150–250 km on the dayside, and it ascends up to about 600 km altitude on the nightside. Note that at certain places the open/closed boundary penetrates into below the O_2^+ production region shown by red (the solar zenith angle range of 45–90°). This means that some of the O_2^+ ions produced may escape. The enlarged plot of the key region (40° < SZA < 100°, 140 km < altitude < 350 km) shows that the open streamlines pass through a pair of production (red) and loss (blue) layers with the loss region encountered after the production layer. Such a combination of O_2^+ production/loss layers is generally a signature of the presence of an upward flow in the Martian ionosphere. The production of O_2^+ at the lower altitude and upward flow from there is because the electron density in the lower ionosphere is less than what causes the recombination loss rate to balance the O_2^+ production rate. A part of the excess O_2^+ transported to higher altitudes is chemically lost, signifying the loss layer on top of the production layer.

One can clearly see that only in the meridian plane for the case with IMF is the O_2^+ production region (colored in red) situated on the open streamlines. This happens at the altitude
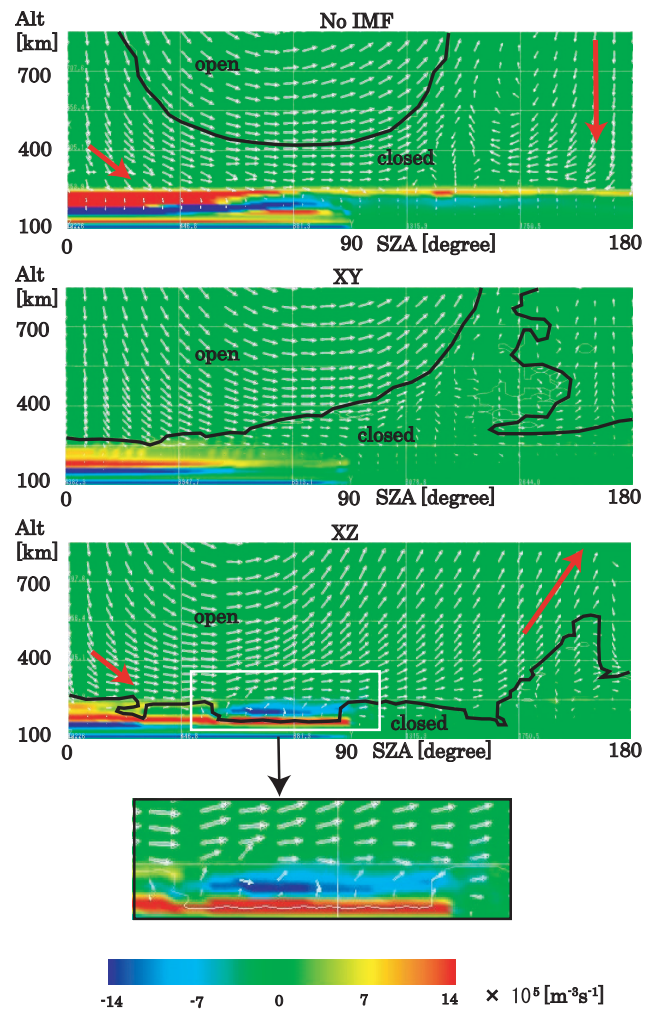

Fig. 10. Contour plots of the net O_2^+ production/loss obtained by our MHD simulation. The arrows on the panels indicate velocity vectors. The top panel corresponds to the values in the case of no IMF. The middle panel corresponds to the values in the equatorial plane containing IMF. The bottom panel corresponds to the values in the meridian plane affected by magnetic tension. An enlargement of the white rectangular area in the bottom panel is shown. These are shown as functions of the solar zenith angle (horizontal axis) and the altitude (vertical axis). The label "open" indicates the region in which the open stream lines exist. The label "closed" indicates the region in which the closed stream lines exist. The red arrows indicate the characteristic flow direction. The flow direction on the nightside is planetward in the case without IMF, while the flow direction on the nightside is anti-planetward in the case with IMF. The flow direction on the dayside is downward in both cases; that is, the solar wind penetrates into the ionosphere.

of 170 km at SZA = 45–90°. There are two issues that cause this to happen. One is the elongation of the O_2^+ production region to SZA = 90°, which is explained above. The other is the severe downward shift of the open/closed demarcation line, which happens because the streamlines that touches the O_2^+ production region do not come back to the ionosphere
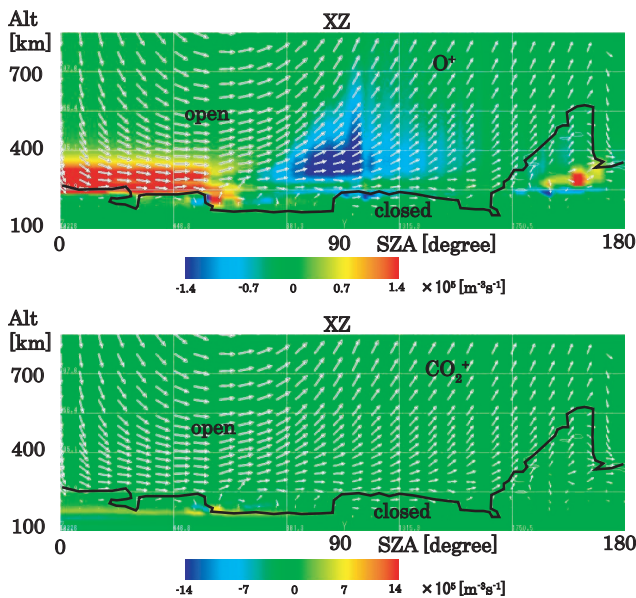
Fig. 11. Contour plots of the net O^+ (upper panel) and CO_2^+ (lower panel) production/loss rates obtained by our MHD simulation in the case of a finite IMF. The format of the figure is the same as that for Fig. 10.

in the nightside. In conclusion, we have shown that, in the case of finite IMF, O_2^+ produced at the altitude of 170 km and SZA = 45–90° find themselves on open streamlines and escape from the planet. As shown in the previous parts, the magnetic tension of the anti-sunward-convecting magnetic field gathers these molecular ions to the poles and then lifts them to higher altitude to form the tail ray.

Having seen that the format of Fig. 10 is eloquent in telling the O_2^+ escape mechanism, we create the same plot for O^+ and CO_2^+ ions. Figure 11 shows the results in the meridian plane for O^+ (upper panel) and CO_2^+ (lower panel), respectively. The O^+ production region (colored in red) is located above 300 km altitude on the dayside and is on open streamlines. It clearly shows that the pick-up from the extended O corona is the major mechanism of the O^+ escape. About 50 % of the whole escape flux of O^+ is produced in the open region above 400 km. As compared with the no IMF case, O^+ escape flux is almost the same. One can see that the CO_2^+ production region at the altitude of 170 km and SZA = 45–90° is on open streamlines. This indicates that the CO_2^+ escape mechanism is the same as that for O_2^+. The production rate of CO_2^+, however, is less, which leads to the smaller escape flux of CO_2^+ shown in Table 2.

4 Discussion and summary

We have shown that O_2^+ and CO_2^+ can escape from the Martian ionosphere in the presence of finite IMF because O_2^+ and

CO_2^+ are shoveled from low-altitude regions of the dayside ionosphere by the magnetic tension. Without IMF, O_2^+ and CO_2^+ transported from the dayside form a vortex in the nightside and return to the ionosphere. With a finite IMF, O_2^+ and CO_2^+ ions transported to the nightside form a ray structure at the center of the tail. They are pulled anti-planetward by the U-shaped field lines, and the ions do not return to the Martian ionosphere. For this process to be effective, IMF-lines need to penetrate into the low-altitude ionosphere where the molecular ions are produced. It is noted that, for the typical solar wind parameter adopted in our simulation, IMF penetrates into the low-altitude ionosphere to shovel the molecular ions.

We have shown that the spatial distribution of plasma in the tail puts on a ray structure at the center. The distribution of ion fluxes observed by MEX at the altitude of 1 R_M on the nightside is shown by Barabash et al. (2007a). They show that the ions including the molecular ions are concentrated at the center of the tail and create a sheet-like structure corresponding to the current sheet in the induced magnetosphere tail. We can find this sheet-like structure in the meridian plane in our simulation. The same tail structure in Venus was observed by Venus Express (VEX) (Fedorov et al., 2011). The observed distribution of ion fluxes is consistent with our simulation result and would signify the effects of the magnetic tension. However, we should point out differences between our simulation result and the observations. The observations suggest that the observed heavy ion escape fluxes are higher in the positive-z hemisphere, which is the direction of the solar wind convection electric field, than in the negative-z hemisphere (Barabash et al., 2007a). Because our simulation is a multispecies MHD code, it does not include the effect of ion-finite gyro radius and asymmetry due to the convection electric field. In our simulation, the distribution of heavy ions is symmetrical to the z direction. The observed asymmetry would be understood by taking into account the finite-radius effect under the z-directed solar wind convection electric field by using multifluid MHD simulation or hybrid simulation, which is out of the scope of the present study. Another difference between our simulation result and the observations is low-energy ions distributed as a ring (like a smile) in the Southern Hemisphere observed by MEX and VEX (Barabash et al., 2007a,b). These ions are observed on the field lines instantly connected to the dayside ionosphere. This escape process does not occur in this paper's results. However, in the case of low solar wind dynamic pressure in our simulation, heavy ions at low energy escape on the field lines in the vicinity of equatorial plane because the convection in the dayside ionosphere is upward and the heavy ions that flow at high-altitude are transported from dayside to nightside. This escape process may indicate the observations of low-energy ions distributed as a ring.

Fränz et al. (2010) suggests that a ratio of O^+/O_2^+ is almost 1 at an altitude of 290–500 km at the terminator. In our

evaluated escape fluxes, the ratio is ~ 2.3 derived from Table 2. The difference of the ratio is due to difference of the evaluated region. The non-thermal O is distributed at an altitude of a few R_M and escapes by pick-up process. Our escape flux includes the ion escape at high altitude because our evaluated region is all simulation boxes. In our simulation, the O^+/O_2^+ ratio at altitude 290–500 km at the terminator is almost 1. This is consistent with their result.

We compared heavy ions escape fluxes in our simulation with the observation of Barabash et al. (2007a) as shown in Table 2. The escape fluxes observed at tail region are consistent with our simulation results. However, the escape fluxes are estimated in the energy range to be more than 30 eV. Because MHD escape rate contains the whole energy range, a realistic MHD escape rate should be larger than the measured values. It is important that we mention this inconsistency. Our MHD model cannot treat the non-MHD escape process such as that of sputtering. We need to consider the non-MHD escape process in order to compare the observed escape flux more carefully. In addition, our simulation model does not include crustal field. The crustal magnetic field can protect the low-altitude ionosphere from IMF. This should reduce the total escape rate provided by the presented mechanism.

Lundin et al. (2009) estimated the escape flux including the low-energy escape fluxes to be less than 50 eV at the terminator region. Those escape fluxes are $O^+ = 2.1 \times 10^{24}$, $O_2^+ = 1.4 \times 10^{24}, CO_2^+ = 3.5 \times 10^{23} \text{ s}^{-1}$. These escape fluxes are larger than our simulation results. Reasons for these differences could be that (1) these escape fluxes were evaluated at the terminator region supposing that these escape fluxes at the terminator were x-axial symmetry and that (2) a part of observed flux could not escape but could return to the nightside ionosphere. Consequently, these values are larger than our simulation results.

We should discuss the limitations of the used multispecies MHD model. In our simulation, all ion species have the same bulk velocity. This supposition is not useful in the case of a high-temperature region such as the solar wind, but it is useful in the case of a low-temperature region such as the ionosphere because bulk velocity of pick-up ions become the background fluid velocity and the gyro radius is proportional to the square root of temperature. Molecular ions are produced at low altitude in the ionosphere. Therefore we could estimate these escape fluxes by integrating production and loss on the open streamline in the ionosphere. However, the molecular ions produced at low altitude are transported to high altitude. At high altitude, the gyro radius becomes longer, and the escape path of these ions would cause asymmetry as mentioned above. Moreover, a part of an ion picked up at high altitude such as O^+ may return to Mars because gyro radius at the solar wind region is a few times the Martian radius. We do not consider the effect of this return.

We have shown the ionosphere density distribution at subsolar point. We should compare our density distribution with the Viking 1 lander observation (Hanson et al., 1977). Density distribution below 250 km is the same as photochemical equivalence, while density distribution above 250 km depends on the solar wind dynamic pressure. Therefore it is difficult to compare our result with the Viking 1 lander observation at SZA = 45° directly. Shinagawa and Cravens (1989) and Fox and Haĉ (2009) simulate the altitude profiles of the ion densities using one-dimensional simulation, and compare with the Viking observation. Shinagawa and Cravens (1989) point out that the ionosphere should have downward velocity and horizontal ion loss due to large-scale horizontal plasma convection in order to explain the observed ion profiles such as O_2^+ and O^+. However, they suggest that the horizontal loss rates are artificially reduced in their model because the horizontal loss is strong when the ionosphere has the downward velocity. Fox and Haĉ (2009) show that their density distribution is consistent with the Viking observation when vertical velocity in the ionosphere is upward. These simulation results indicate that it needs the ion loss due to horizontal or upward convection in the ionosphere to explain the observation profile. In our simulation under the used solar wind parameters, the density profiles at SZA = 60° in the meridian plane is in good agreement with the Viking 1 lander observation because ions such as O_2^+ and O^+ are lost due to the horizontal and upward convection produced by magnetic tension. The density profiles at SZA = 45°, where the vertical velocity is downward, in our simulation are smaller than the densities of the Viking observation because the horizontal ion loss is strong. In order to reproduce the Viking density profiles at SZA = 45° in our simulation, we need to calculate a case of low solar wind dynamic pressure in which the vertical convection is upward in the ionosphere.

We have also studied how the escape fluxes of different ion species depend on the solar wind dynamic pressure. Two additional cases with IMF, in which the solar wind density and thus the dynamic pressure are switched to 0.1 and 10 times the value used in the run shown above, have been performed. The escape flux of O^+ is found to be in direct proportion to the solar wind density. This is understandable if we note that the rate of electron impact ionization of O corona is proportional to the solar wind electron density. What is interesting is that the escape flux of the molecular ions (O_2^+ and CO_2^+) has a weaker dependence on the solar wind pressure than O^+. The escape flux of O_2^+ varies from 2.0×10^{23} to $9.0 \times 10^{23} \text{ s}^{-1}$ when the solar wind density is changed by 2 orders of magnitude. The molecular ions are produced in the low-altitude region where CO_2 is abundant. When the solar wind density is elevated by a factor of 10, since the open/closed boundary is already located at below 200 km altitude, where strong collisions with neutrals exist, it is not possible to lower the boundary substantially. The escape flux is only slightly increased. When the solar wind density is reduced to 1/10, under the low dynamic pressure, the convection in the dayside ionosphere becomes upward (Jin, 2004). Therefore O_2^+ and CO_2^+ flow out from the low-altitude regions in the dayside

ionosphere along the open streamlines. However, since the ions are produced deep in the ionosphere and the upward speed is low (less than $100\,\mathrm{m\,s^{-1}}$) at low altitudes, the ions are quickly lost by recombination before reaching higher altitudes. As a result, the escape flux is slightly reduced.

We compare the obtained solar wind dependence of ion escape fluxes with observations. Lundin et al. (2008) suggested that there is a strong correlation between the solar wind dynamic pressure and the planetary ion loss rate. They focused on the heavy ions in the energy range of 30–800 eV, and reported that the total escape flux increases from 6.0×10^{23} to $6.0 \times 10^{24}\,\mathrm{s^{-1}}$ as the solar wind pressure increases from 0.1 to 10 times the nominal value. However, our simulation result indicates that the total (O^+, O_2^+ and CO_2^+) escape flux increases from 2.0×10^{23} to $9.0\times10^{24}\,\mathrm{s^{-1}}$ for the same range of solar wind pressure variation. The reason why the observed variation is smaller may be that the upper limit of the energy range dealt in the observation is not high enough to include those O^+ that are picked up at relatively high altitudes where the flow speed is high. When the O^+ flux is not fully included, the contribution of O_2^+ and CO_2^+, which have a weaker dependence on the solar wind pressure, to the total ion escape flux becomes more substantial.

Here let us discuss the molecular ion (O_2^+) escape for the Venus case. When the solar wind dynamic pressure is high, IMF penetrates into the dayside ionosphere and the molecular ions' escape can be expected. In order to simulate the Venus case, we change the neutral atmospheric model from Mars to Venus. The solar wind parameter and photoionization frequencies are arranged appropriately as well. In the results, we have found that the escape flux of O_2^+ is estimated to be $\sim 10^{23}\,\mathrm{s^{-1}}$ when the solar wind dynamic pressure is high; that is, when IMF penetrates into the dayside ionosphere. Meanwhile, the O^+ escape flux for this case is $\sim 10^{25}\,\mathrm{s^{-1}}$, which is larger by an order of magnitude than the Martian case. The reason for this enhanced O^+ flux is simply that the solar wind electron density at Venus is larger than at Mars. Barabash et al. (2007b) show that the escape of O^+ from Venus is observed, while molecular ion (such as O_2^+ and CO_2^+) escape is not observed. Our simulation results show that the O_2^+ and CO_2^+ do escape at the same rate as for the Martian case when the solar wind dynamic pressure is high. The molecular ion escape, however, would not have been detected by VEX observation because it would have been masked by the far larger flux of O^+.

References

Acuña, M. H., Connerney, J. E. P., Wasilewski, P., Lin, R. P., Anderson, K. A., Carlson, C. W., McFadden, J., Curtis, D. W., Mitchell, D., Reme, H., Mazelle, C., Sauvaud, J. A., D'Uston, C., Cros, A., Medale, J. L., Bauer, S. J., Cloutier, P., Mayhew, M., Winterhalter, D., and Ness, N. F.: Magnetic field and plasma observation at Mars: Initial results of the Mars Global Surveyor mission, Science, 279, 1676–1680, 1998.

Acuña, M. H., Connerney, J. E. P., Ness, N. F., Lin, R. P., Mitchell, D., Carlson, C. W., McFadden, J., Anderson, K. A., Reme, H., Mazelle, C., Vignes, D., Wasilewski, P., and Cloutier, P.: Global distribution of crustal magnetization discovered by the Mars Global Surveyor MAG/ER experiment, Science, 284, 790–793, 1999.

Anicich, V. G.: Evaluated bimolecular ion-molecule gas phase kinetics of positive ions for use in modeling planetary atmospheres, cometary comae, and interstellar clouds, J. Phys. Chem. Ref. Data, 22, 1469–1569, 1993.

Barabash, S., Fedorov, A., Lundin, R., and Sauvaud, J.-A.: Martian Atmospheric Erosion Rates, Science, 315, 501–503, 2007a.

Barabash, S., Fedorov, A., Sauvaud, J. J., Lundin, R., Russell, C. T., Futaana, Y., Zhang, T. L., Andersson, H., Brinkfeldt, K., Grigoriev, A., Holmström, M., Yamauchi, M., Asamura, K., Baumjohann, W., Lammer, H., Coates, A. J., Kataria, D. O., Linder, D. R., Curtis, C. C., Hsieh, K. C., Sandel, B. R., Grande, M., Gunell, H., Koskinen, H. E. J., Kallio, E., Riihela, P., Sales, T., Schmidt, W., Kozyra, J., Krupp, N., Franz, M., Woch, J., Luhmann, J., McKenna-Lawlor, S., Mazelle, C., Thocaven, J.-J., Orsini, S., Cerulli-lrelli, R., Mura, M., Milillo, M., Maggi, M., Roelof, E., Brandt, P., Szego, K., Winningham, J. D., Frahm, R. A., Scherrer, J., Sharber, J. R., Wurz, P., and Bochsler, P.: The loss of ions from Venus through the plasma wake, Nature, 450, 650–653, 2007b.

Bößwetter, A., Bagdonat, T., Motschmann, U., and Sauer, K.: Plasma boundaries at Mars: a 3-D simulation study, Ann. Geophys., 22, 4363–4379, doi:10.5194/angeo-22-4363-2004, 2004.

Brecht, S. H.: Hybrid simulation of the magnetic topology of Mars, J. Geophys. Res., 102, 4743–4750, 1997.

Brecht, S. H., Ferrante, J. R., and Luhmann, J. G.: Three-dimensional simulation of the solar wind interaction with Mars, J. Geophys. Res., 98, 1345–1357, 1993.

Cloutier, P. A., Law, C. C., Crider, D. H., Walker, P. W., Chen, Y., and Acuña, M. H., Connerney, J. E. P., Lin, R. P., Anderson, K. A., Mitchell, D. L., Carlson, C. W., McFadden, J., Brain, D. A., Reme, H., Mazelle, C., Sauvaud, J. A., D'Uston, C., Vignes, D., Bauer, S. J., and Ness, N. F.: Venus-like interaction of the solar wind with Mars, Geophys. Res. lett., 26, 2685–2688, 1999.

Cravens, T. E., Shinagawa, H., and Nagy, A. F.: The evolution of large-scale magnetic fields in the ionosphere of Venus, Geophys. Res. lett., 11, 267–270, 1984.

Fedorov, A., Barabash, S., Sauvaud, J.-A., Futaana, Y., Zhang, T. L., Lundin, R., and Ferrier, C.: Measurements of the ion escape rates from Venus for solar minimum, J. Geophys. Res., 116, A07220, doi:10.1029/2011JA016427, 2011.

Fox, J. L. and Haċ, A. B.: Photochemical escape of oxygen from Mars: A comparison of the exobase approximation to a Monte Carlo method, Icarus, 204, 527–544, 2009.

Fränz, M., Dubinin, E., Nielsen, E., Wocha, J., Barabash, S., Lundin, R., and Fedorov, A.: Transterminator ion flow in the Martian ionosphere, Plant. Space Sci., 58, 1442–1454,

doi:10.1016/j.pss.2010.06.009, 2010.

Hanson, W. B. and Mantas, G. P.: Viking electron temperature measurements: Evidence for a magnetic field in the Martian ionosphere, J. Geophys. Res., 93, 7538–7544, 1988.

Hanson, W. B., Sanatani, S., and Zuccaro, D. R.: The Martian ionosphere as observed by the Viking retarding potential analyzers, J. Geophys. Res., 82, 4351–4363, 1977.

Jin, H.: IMF penetration into the ionospheres of Venus and Mars, PhD thesis, Univ. of Tokyo, Tokyo, 2004.

Jin, H., Maezawa, K., and Mukai, T.: Effects of charge exchange and electron impact ionization on the formation of the magnetic pileup boundary at Mars, J. Geophys. Res., 111, A05306, doi:10.1029/2005JA011127, 2006.

Jin, H., Maezawa, K., and Mukai, T.: The critical wind pressure for IMF penetration into the Venus ionosphere, J. Geophys. Res., 113, A02309, doi:10.1029/2007JA012725, 2008.

Kallio, E. and Janhunen, P.: Atmospheric effects of proton precipitation in the martian atmosphere and its connection to the Mars-solar wind interaction, J. Geophys. Res., 106, 5617–5634, 2001.

Kallio, E. and Janhunen, P.: Ion escape from Mars in a quasi-neutral hybrid model, J. Geophys. Res., 107, 1035, doi:10.1029/2001JA000090, 2002.

Kim, J., Nagy, A. F., Fox, J. L., and Cravens, T. E.: Solar cycle variability of hot oxygen atoms at Mars, J. Geophys. Res., 103, 29339–29342, 1998.

Krasnopolsky, V. A.: Solar cycle variations of the hydrogen escape rate and the CO mixing ratio on Mars, Icarus, 101, 313–332, 1993.

Krasnopolsky, V. A. and Gladstone, G. R.: Helium on Mars: EUVE and PHOBOS data and implications for Mars' evolution, J. Geophys. Res., 101, 15765–15772, 1996.

Luhmann, J. G., Russell, C. T., and Elphic, R. C.: Time scale for the decay of induced large-scale magnetic fields in the Venus ionosphere, J. Geophys. Res., 89, 362–368, 1984.

Lundin, R., Zakharov, A., Pellinen, R., Hultqvist, B., Borg, H., Dubinin, E., Barabash, S., Pissarenko, N., Koskinen, H., and Liede, I.: First measurements of the ionospheric plasma escape from Mars, Nature, 341, 609–612, 1989.

Lundin, R., Barabash, S., Fedorov, A., Holmström, M., Nilsson, H., Sauvaud, J.-A., and Yamauchi, M.: Solar forcing and planetary ion escape from Mars, Geophys. Res. lett., 35, L09203, doi:10.1029/2007.GL.032884, 2008.

Lundin, R., Barabash, S., Holmström, M., Nilsson, H., Yamauchi, M., Dubinin, E. M., and Fraenz, M.: Atmospheric origin of cold ion escape from Mars, Geophys. Res. lett., 36, L17202, doi:10.1029/2009GL039341, 2009.

Ma, Y. and Nagy, A. F.: Ion escape fluxes from Mars, Geophys. Res. lett., 34, L08201, doi:10.1029/2006GL029208, 2007.

Ma, Y., Nagy, A. F., Sokolov, I. V., and Hansen, K. C.: Three-dimensional, multispecies, high spatial resolution MHD studies of the solar wind interaction with Mars, J. Geophys. Res., 109, A07211, doi:10.1029/2003JA010367, 2004.

Modolo, R., Chanteur, G. M., Dubinin, E., and Matthews, A. P.: Influence of the solar EUV flux on the Martian plasma environment, Ann. Geophys., 23, 433–444, doi:10.5194/angeo-23-433-2005, 2005.

Modolo, R., Chanteur, G. M., Dubinin, E., and Matthews, A. P.: Simulated solar wind plasma interaction with the Martian exosphere: influence of the solar EUV flux on the bow shock and the magnetic pile-up boundary, Ann. Geophys., 24, 3403–3410, doi:10.5194/angeo-24-3403-2006, 2006.

Nagy, A. F. and Cravens, T. E.: Hot oxygen atoms in the upper atmospheres of Venus and Mars, Geophys. Res. lett., 15, 433–435, 1988.

Najib, D., Nagy, A. F., Tóth, G., and Ma, Y.: Three-dimensional, multifluid, high spatial resolution MHD studies of the solar wind interaction with Mars, J. Geophys. Res., 116, A05204, doi:10.1029/2010JA016272, 2011.

Phillips, J. L., Luhmann, J. G., and Russell, C. T.: Growth and maintenance of large-scale magnetic fields in the dayside Venus ionosphere, J. Geophys. Res., 89, 10676–10684, 1984.

Russell, C. T. and Vaisberg, O.: The Interaction of the Solar Wind with Venus, in: Venus, Univ. of Arizona Press, 1983.

Schunk, R. W. and Nagy, A. F.: Ionospheres: Physics, Plasma Physics, and Chemistry, Cambridge Univ. Press, New York, 2000.

Shimazu, H.: Three-dimensional hybrid simulation of magnetized plasma flow around an obstacle, Earth Planets Space, 51, 383–393, 1999.

Shimazu, H.: Three-dimensional hybrid simulation of solar wind interaction with unmagnetized planets, J. Geophys. Res., 106, 8333–8342, 2001.

Shinagawa, H.: A two-dimensional model of the Venus ionosphere: 1. Unmagnetized ionosphere, J. Geophys. Res., 101, 26911–26919, 1996a.

Shinagawa, H.: A two-dimensional model of the Venus ionosphere: 2. Magnetized ionosphere, J. Geophys. Res., 101, 26921–26930, 1996b.

Shinagawa, H. and Cravens, T. C.: A one-dimensional multi-species magnetohydrodynamic model of the dayside ionosphere of Venus, J. Geophys. Res., 93, 11263–11277, 1988.

Shinagawa, H. and Cravens, T. C.: A one-dimensional multispecies magnetohydrodynamic model of the dayside ionosphere of Mars, J. Geophys. Res., 94, 6506–6516, 1989.

Shinagawa, H., Cravens, T. C., and Nagy, A. F.: A one-dimensional time-dependent model of the magnetized ionosphere of Venus, J. Geophys. Res., 92, 7317–7330, 1987.

Tanaka, T. and Murawski, K.: Three-dimensional MHD simulation of the solar wind interaction with the ionosphere of Venus: Results of two-component reacting plasma simulation, J. Geophys. Res., 102, 19805–19821, 1997.

Torr, M. R. and Torr, D. G.: Ionization frequencies for solar cycle 21: Revised, J. Geophys. Res., 101, 6675–6678, 1985.